Ducted wind turbines in yawed flow: A numerical study

Vinit Dighe[1], Dhruv Suri[2], Francesco Avallone[1], and Gerard van Bussel[1]

[1]Wind Energy Research Group, Faculty of Aerospace Engineering, Technological University of Delft, Netherlands
[2]Renewable Energy Research Group, Department of Aeronautical and Automobile Engineering, Manipal Institute of Technology, India

Correspondence: Vinit Dighe (v.v.dighe@tudelft.nl)

Abstract. Ducted Wind Turbines (DWTs) can be used for energy harvesting in urban areas where non-uniform flows are caused by the presence of buildings or other surface discontinuities. For this reason, the aerodynamic performance of DWTs in yawed flow conditions must be characterized. A numerical study to investigate the characteristics of flow around two DWT configurations using a simplified duct-actuator disc (AD) model is carried out. The analysis shows that the aerodynamic performance of a DWT in yawed flow is dependent on the mutual interactions between the duct and the AD; an interaction that changes with duct geometry. It is found that the duct cross-section camber returns a gain in performance up to a specific yaw angle; thereafter any further increase of yaw angle results in a performance drop.

1 Introduction

Global energy demand is expected to more than double by 2050 owing to the growth in population and economy (Gielen et al., 2019). The global wind power capacity quadrupled in less than a decade reaching 597 Gigawatt by the end of 2018 compared to 120 Gigawatt in 2008 (Dupont et al., 2018). Wind turbines are typically installed away from populated areas considering the enforced visual and noise regulations. This necessitates the transfer of electricity via grids over large distances, which increases the levelized cost of electricity (LCOE). However, the integration of wind turbines into urban areas is challenging; the presence of buildings, trees and surface discontinuities lead to lower wind speed, non-uniform inflow and larger turbulent fluctuations compared to open fields. To address these challenges, design modifications of wind turbines, suitable for operation in an urban setting is required.

A possible technological solution to extract wind energy in urban areas is represented by Ducted Wind Turbines (DWTs). DWTs increase energy extraction with respect to conventional horizontal axis wind turbines (HAWTs) for a given turbine radius and free-stream velocity (van Bussel, 2007). DWTs are constituted of a turbine and a duct (also named as diffuser or shroud); the role of the latter is to increase the flow rate through the turbine relative to a similar turbine operating in the open atmosphere, thus increasing the generated power. There is more than one explanation for how this occurs: (i) the duct forces an expansion of flow downstream of the turbine beyond what is attainable for a bare wind turbine. This provides a reduced pressure behind the turbine, and increase the total mass flow through the turbine (van Bussel, 2007) and (ii) the sectional lift force of the duct when directed towards the turbine plane, the associated circulation (see Figure 1) of the duct increases the mass flow through the turbine (de Vries, 1979). A significant amount of literature on DWTs, based on the combined use of
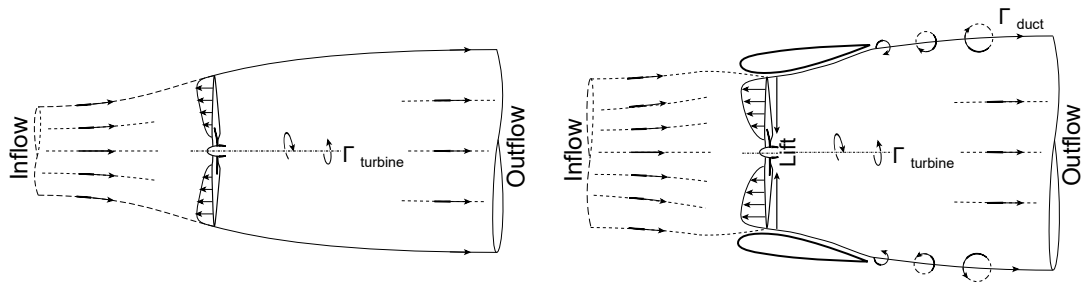
Figure 1. Schematic of stream-tube model for a bare turbine (left) and DWT (right). The bound circulation from the turbine blades and the duct surface is denoted by τ

theoretical, numerical and experimental techniques, exists (Igra, 1981; Gilbert and Foreman, 1983; Abe et al., 2005; Toshimitsu et al., 2008; Werle and Presz, 2008; Khamlaj and Rumpfkeil, 2017). Questions over the performance of DWTs in yawed flow remain, however.

Igra (1981) studied experimentally the effects of yaw on the performance of DWTs. Eight geometries were investigated using different duct profiles and an actuator disc (AD) model to represent the turbine. The eight configurations differed in the duct expansion ratio, i.e., the ratio of exit area of the duct to the turbine area. The AD with a thrust coefficient of approximately 0.5 was chosen. It was found that when the duct expansion ratio was less than 4.5, little or no difference in the power output was measured up to a yaw angle of $\pm\,30°$ while any further increase in yaw resulted in power reduction. On the other hand, when the duct expansion ratio was higher than 4.5, the generated power decreased even for small yaw angles. Igra explained that the yaw insensitivity, for the low duct expansion ratio configurations, is due to the lift force increase by the annular duct section. The author did not provide any explanation to further clarify the physics behind performance drop for large duct expansion ratio. On the same line, researchers from Grumman Aerospace tested a bare turbine and two DWT models (named as Baseline DAWT and DAWT 45) varying the yaw angle up to 40° with increments of 10° (Gilbert and Foreman, 1983). Both the Baseline DAWT and DAWT 45 models showed a negligible change in the power up to a yaw angle of 30°, and a drastic reduction in power at yaw angle of 40°. Surprisingly, the bare turbine also demonstrated no dependence on the yaw angle up to 30°. They stated that this was due to the long center-body configuration, similar in all the three designs, that helped channeling the incoming flow towards the upwind turbine blade and at the same time shielding the downwind turbine blade, thus offering an insensitivity to yaw. However, in a follow up paper (Foreman and Gilbert, 1983) they stated that these yaw tests were inconclusive whether the yaw insensitivity was due to the center-body effect or the duct geometry itself. More recently, Phillips et al. (2002) combined experimental and numerical analysis to study DWTs under yawed flow. They concluded that the power increase for a DWT in yawed flow can only be achieved with a slotted duct design (named as Mo), with the added mass flow of air through the slot increasing the boundary layer flow control and preventing flow separation over the suction side (inner surface) of the duct under severe yaw misalignment. The above literature, due to the contrasting nature of the conclusions, lacks clarity on the aerodynamics of DWTs in yawed flow, and particularly on the effect of the duct geometry on the aerodynamic performances.

The goal of this paper is to focus on the latter; this is performed using unsteady Reynolds Averaged Navier Stokes (URANS) CFD simulations.

In all the simulations presented in this article, the turbine is represented using a numerical actuator disc (AD) model, a method widely used to model the principal effects of turbine in a simplified manner. In the AD model, the turbine forces are assumed to be distributed evenly along the AD; hence, the influence of the blades is taken as an integrated quantity in the azimuthal direction. The effects of distributed forces for real turbine geometries are modelled using more sophisticated techniques like actuator line (Troldborg, 2009) or actuator surface (Shen et al., 2009) methods. Incorporating the real turbine geometries, which would necessarily have to be different for ducted and for bare operation, would confuse turbine and duct effects, preventing a proper analysis of DWTs in yawed flow. Thus, the AD approach is chosen deliberately for this investigation, so as to study the impact of duct shapes, and not the specific performance of a rotor within a duct. The effects of real turbine within different duct geometries are studied in a subsequent publication by the authors, see Dighe et al. (2020). The numerical AD method has been extensively validated, see for example Dighe et al. (2019a, b). The numerical AD model has been been applied by Mikkelsen and Sørensen (2001) to study the flow on a horizontal axis wind turbine in axial and yawed flow conditions. The numerical predictions agree reasonably well, both in axial and yawed flow conditions, when compared to the measurements on the Tjæreborg 2MW field turbine. This model is also employed by Tongchitpakdee et al. (2005) to study yaw; the NASA-Ames experiments of the NREL Phase VI turbine are modeled for yaw angles from $0°$ to $45°$ to find reasonable agreement with the experiments.

The paper is organized as follows. Section 2 reports the non-dimensional coefficients adopted for characterizing the aerodynamic performance of the duct-AD model, both under non-yawed and yawed flow conditions. Section 3 describes the numerical settings and parameters with the description of the duct profiles chosen for the current investigation. Section 4 reports the numerical validation study. Insights on the aerodynamic performance coefficients with respect to yawed flow will be discussed in section 5, together with flow analysis. Finally, the most relevant results are summarized in the conclusions.

2 Duct - AD flow model

The turbine is modelled by a flat AD. The AD exerts a constant thrust force T_{AD}, calculated across the AD surface S_{AD}, which corresponds to a non-dimensional thrust force coefficient:

$$C_{T_{AD}} = \frac{T_{AD}}{0.5\rho U_\infty{}^2 S_{AD}}, \tag{1}$$

where ρ is the fluid density and U_∞ is the free-stream velocity.

To generate T_{AD}, a uniform pressure drop is present across the AD surface, $T_{AD} = \Delta p \times S_{AD}$. The pressure drop Δp is taken from experiments (Tang et al., 2016) and is given as an input parameter to the numerical simulations. The mean velocity across the AD radial plane, which is a function of AD thrust coefficient $U_{AD_0} = f(C_{T,AD})$, can be expressed by integrating
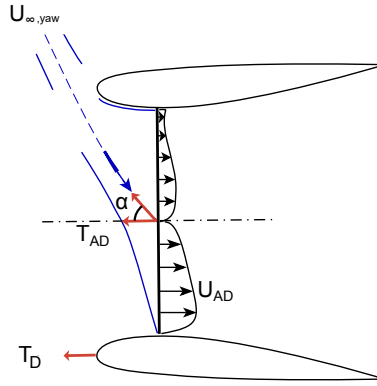
Figure 2. Schematic of yawed flow around a duct-AD model

the difference of the free-stream velocity component U_x across the AD surface:

$$\frac{U_{AD_0}}{U_\infty} = \frac{1}{S_{AD}} \oint_{S_{AD}} U_x dS. \tag{2}$$

Using Eqs. 1 and 2, the power coefficient for a bare AD reads:

$$C_{P_o} = \frac{U_{AD_o}}{U_\infty} C_{T_{AD}}. \tag{3}$$

5   The subscript o has been adopted for quantities evaluated for bare AD configuration.

For a duct-AD configuration, an additional thrust force exerted by the duct on the flow, or vice-versa, appears. Then, the total thrust force T is the vectorial sum of the AD thrust force T_{AD}, and the duct thrust force T_D, given by:

$$T = T_{AD} + T_D. \tag{4}$$

The total thrust coefficient is then defined as:

10    $$C_T = C_{T_{AD}} + C_{T_D}. \tag{5}$$

Note that the duct thrust coefficient C_{T_D} is normalized with the AD area S_{AD} to facilitate direct addition to the AD thrust coefficient $C_{T_{AD}}$ for calculating the total thrust coefficient C_T. Then, the mean velocity at the AD for a duct-AD model is a bivariate function of AD thrust coefficient and the duct thrust coefficient: $U_{AD} = f(C_{T_{AD}} + C_{T_D}) = f(C_T)$. Similar to Eq. 3, the power coefficient for the duct-AD model, using S_{AD} as the reference area, becomes:

15    $$C_P = \frac{U_{AD}}{U_\infty} C_T. \tag{6}$$

The power coefficient expression in Eq. 6 challenges the well-known Lanchester–Betz–Joukowsky limit of $\frac{16}{27}$ for maximum power coefficient obtainable for a HAWT. This should not appear like a surprising result, since, the mass flow of air swallowed in the presence of a duct is greater due to the additional thrust force C_{T_D} offered by the duct. The above relations are also valid for a DWT under yawed flow condition. Figure 2 shows the schematic of flow around the duct-AD model, where α is the yaw

20   angle relative to the incident free-stream direction.
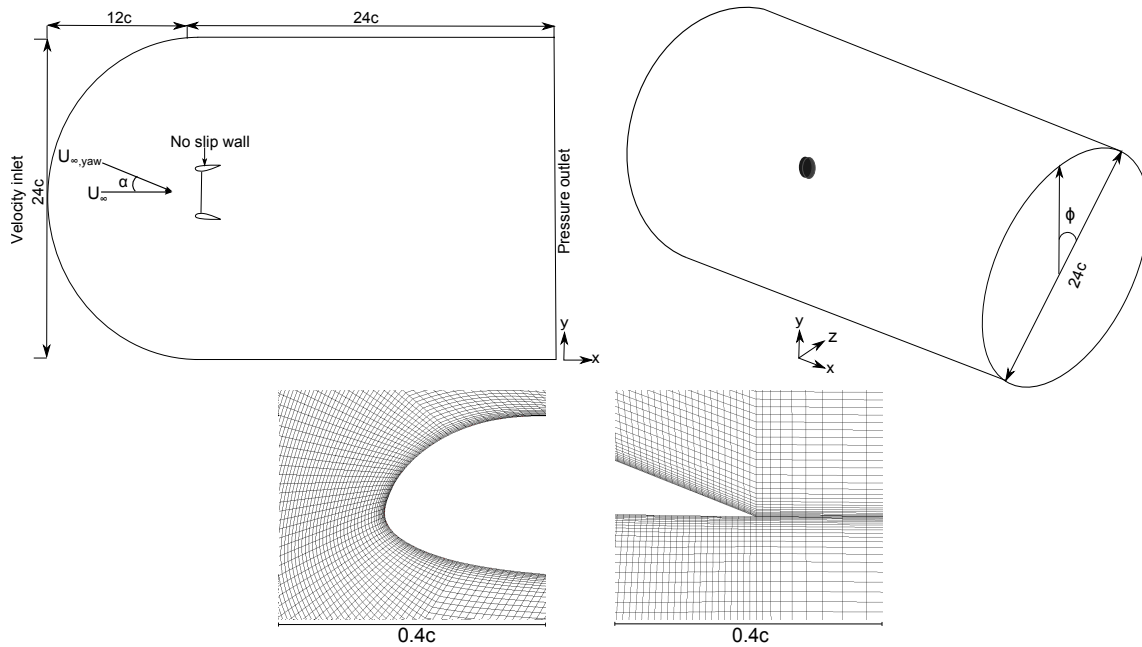
Figure 3. Computational domain showing the boundary conditions employed (top). The lengths are normalized with the duct chord length c. Representative, not to scale. Computational grid surrounding the leading and trailing edge of the duct (bottom).

3 Methodology and Computational Setup

In this study, a commercial CFD solver ANSYS Fluent® is employed for solving the governing flow equations. The solver utilizes the unsteady Reynolds-averaged Navier-Stokes (URANS) formulation. Large flow separation regions are expected for DWTs in yawed flow. Flow solutions obtained using steady RANS formulation for DWTs with large yaw angles did not
5 converge or even diverge. Using URANS formulation, the goal is to capture the asymptotic behavior (quasi-steady state) of the flow in order to reach a converged solution. The k-ω shear stress transport (SST) model is employed for the turbulence closure scheme. Apsley and Leschziner (2000) investigated the ability of various second-order closure models to predict separated flows in a duct and compared them to experimental data. $k - \omega$ SST model returns better predictions than the other second-order closure models with regards to approximating the unsteady flow in the velocity profiles of the duct. Moreover, Shives and
10 Crawford (2012) investigated the application of different closure models for modelling ducted turbine flows. It was concluded that $k - \omega$ SST model outperforms the other first and second-order closure models. A pressure-based coupled solver was selected with a second order implicit transient formulation for improved accuracy. All solution variables were solved via second order upwind discretisation scheme.

In order to evaluate the numerical duct-AD model in nearly unconstrained flow, the computational domain extends $12c$
15 upstream and $24c$ downstream, where c is the duct chord length. The distances are found to be safe choices to minimize the effects of blockage and uncertainty in the boundary conditions on the results. Using the finite volume method, the computational

domain is discretized spatially into finite number of small control volumes known as grid. The grid have been generated using the commercial software ANSYS ICEM CFD. For the present computations, a C-grid structured zonal approach is chosen, see Figure 3, which proved advantageous in the case of a curved boundary, i.e. duct's leading edge. The C-shaped loop terminates in the wake region. The computational grid consists of quadrilateral cells with maximum y^+ value of ≈ 1 on the duct wall.

5 A 3D grid is created by extruding the 2D grid using 100 grid points in azimuthal direction ϕ using the surface grid extrusion technique (ANSYS, 2018). Boundary conditions are: uniform velocity at the inlet, zero gauge static pressure at the outlet, no-slip walls for duct surfaces. The numerical study is performed at a fixed Re of 4.5×10^5. The influence of AD is included into the domain as an additional body force acting opposite to the direction of flow. This is achieved using a reverse fan boundary condition in ANSYS Fluent®. For a uniform thrust loading, the thrust force is given by:

$$T_{AD} = 0.5 C_{T_{AD}} \rho U_\infty^2, \tag{7}$$

where $C_{T_{AD}}$ is calculated from a semi-empirical relation of pressure drop curve and the velocity at the AD obtained from wind tunnel experiments. The fluid is air with fluid density $\rho = 1.276 \frac{kg}{m^3}$ and dynamic viscosity $\mu = 1.722 \times 10^{-5} \ Pa{\cdot}s$. Values of free-stream velocity U_∞ and turbulence intensity I are chosen for consistency with the wind tunnel experiments. To establish

15 yawed inflow conditions, the flow is rotated around the center-line axis by yaw angle α for different test cases.

The simulations were advanced through time with a CFL (Courant) number of one, which resulted in a time-step of approximately 2.67×10^{-4} s. A typical converged 2D URANS solution with approximately 0.1 million mesh elements is obtained in roughly 30 minutes on a quad-core work-station desktop computer. The converged 3D URANS solution with approximately 10 million mesh elements is obtained in roughly 54 hours on a quad-core work-station desktop computer.

20 ## 4 Numerical verification and validation

For validating the numerical approach, experiments carried out by Igra (1981) on a duct-AD geometry (3-dimensional) are simulated. Igra's experiments were conducted in the subsonic wind tunnel of the Israel Aerospace Industry (formerly Israel Aircraft Industry); this tunnel has a large test section and it measures 3.6 m × 2.6 m.

A schematic of the cross-section geometry (named as Model B) is shown in Figure 4(a). The longitudinal cross-section of the

25 duct is a NACA 4412 airfoil. The leading edge of the duct is rotated by $2°$ with respect to the free-stream direction, resulting in a duct expansion ratio (area of duct exit/area of the AD) of 1.54. A uniformly loaded AD model with $C_{T_{AD}} = 0.434$ is used to represent the turbine. The experimental data set consists of: static pressure distribution at different axial and radial positions, and forces generated by the duct surface for a range of flow angles. During the experiments, the inflow velocity was set at $U_\infty = 32$ m/s. Following Igra (1981), the wall interference and blockage correction can be ignored. The experimental data is reported

30 in terms of the augmentation factor $r = \frac{C_P}{C_{P_o}}$, which expresses the ratio between the power coefficient of the duct-AD model and the power coefficient of the bare AD model when both the models bear the same AD and similar operating conditions.

(a) (b)
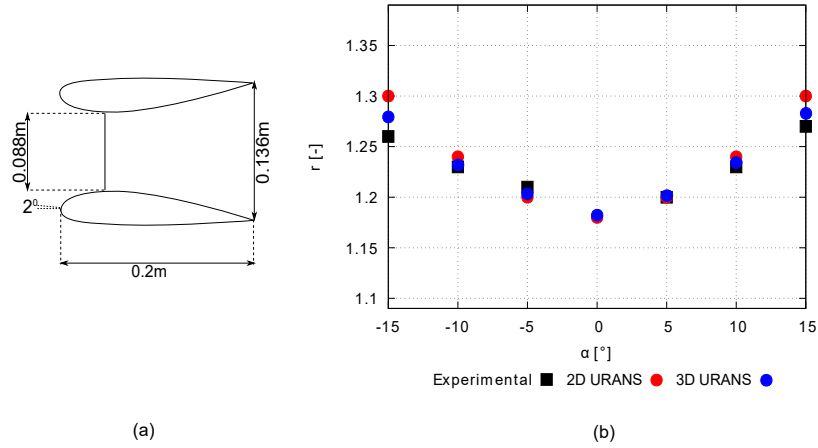
Figure 4. A schematic cross-section layout of the three dimensional experimental model used for the numerical validation study (a), and comparison between experimental findings (Igra, 1981) and the CFD results (b).
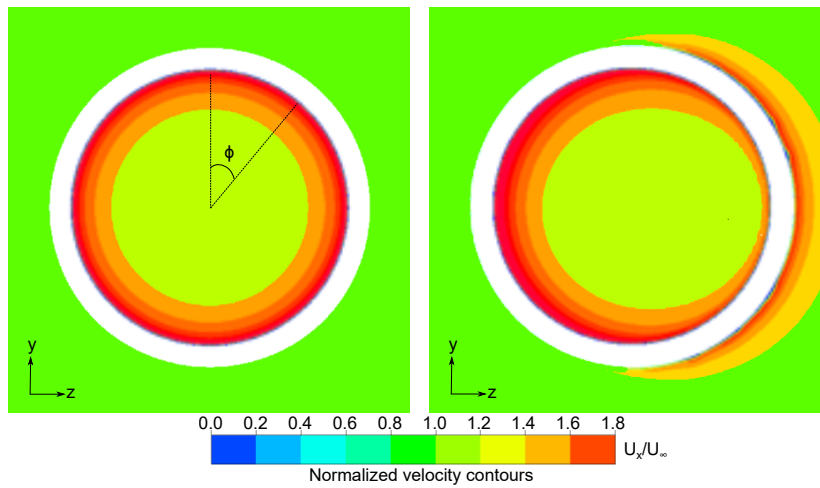
Figure 5. Contours of time-averaged non-dimensional free-stream velocity U_x/U_∞ measured at the AD location located in the $y-z$ plane for Model B in (left) non-yawed inflow and (right) yawed inflow, $\alpha = 10^\circ$.

A good agreement between the CFD simulations and the experimental findings is found in Figure 4(b). The deviation between the CFD and the experimental findings increase with increasing values of α, especially for 2D URANS calculations. The differences in the 2D and 3D CFD results can be explained by looking at the flow field obtained using 3D URANS simulations. Figure 5 shows the time-averaged velocity contours of non-dimensional axial velocity $\frac{U_x}{U_\infty}$ in the $y - z$ plane at the AD location for Model B in non-yawed (left) and yawed (right) inflow conditions. Time averaging is performed after convergence is reached. Because of the yaw angle ($\alpha = 10°$), an asymmetric flow field is present, thus the velocity at the AD plane changes with the azimuthal angle Φ. Here, the azimuthal angle Φ is defined as positive in the clockwise direction when looking from upwind, with zero when oriented in the positive y direction, see Figure 5 (left). The main difference between the two results is due to fact that the C_P (equation 6) obtained from 3D URANS simulations uses the azimuthally averaged streamwise velocity component, while the results from 2D simulations do not account for the gradual variation with Φ. However, as shown in the comparsion, the three dimensional azimuthal effects are negligible when comparing r. It is important to highlight that the maximum deviation between 2D URANS results and experimental findings is less than 5% for $\alpha = \pm 15°$.

For an additional validation of the AD approach, numerical results obtained using 2D and 3D URANS are compared with the experimental study reported by Ten Hoopen (2009). The study was conducted using the full scale DonQi® DWT model in non-yawed inflow condition (see Figure 6). Experiments were conducted in the closed-loop open-jet (OJF) wind tunnel facility at the Delft University of Technology. The average thrust coefficient of the turbine $C_{T_{turbine}}$ was measured in the experimental study to be 0.689; this value is chosen to model $C_{T_{AD}}$ for the results presented. Figure 6 shows the comparison of the normalized free-stream velocity $\frac{U_x}{U_\infty}$ measured behind the turbine blade at $x/c = 0.37$ in the radial direction y. Transition was not forced but the experimental model has a noise damper, see Figure 6, which acts as rough surface that forces transition to turbulence; this has not been replicated numerically. The computed velocity profiles preserves the overall shape, with the relative difference, calculated lower than 10%, which is within the experimental uncertainty and also attributed to the absence of discrete blades and their related effects such as tip vortices, wake rotation and an accelerated mixing of the flow through the DWT with the external flow.

The 2D URANS approach gives results of reasonable accuracy when compared to the 3D URANS approach. An additional numerical verification exercise of the 2D URANS approach is performed, where the results are compared to a full-scale DWT numerical model. It is not reported herein for the sake of brevity; please refer to Appendix A. The computing cost issued by going from 2D URANS to 3D URANS does not justify the scope of the current study, where the effects of distributed AD loading, wake rotation and divergence are totally ignored. Having said that, the 2D URANS approach combined with numerical duct-AD model has been adopted for the results presented, hereinafter.

A grid independence analysis has been carried out for the 2D grid using three grid sizes, where the refinement factor in each direction is 1.5. Refinement factor is defined as the rate at which the grid size increases in the direction normal to the surface of the wall (duct surface). The duct thrust force coefficient C_{T_D} is taken as reference for the convergence analysis. The results of the grid independence study are shown in Table 1. Convergence is reached for the medium refined grid, where the C_{T_D} value fluctuates less than 0.0003%, and similar grid refinement is used in the numerical investigation, hereinafter.
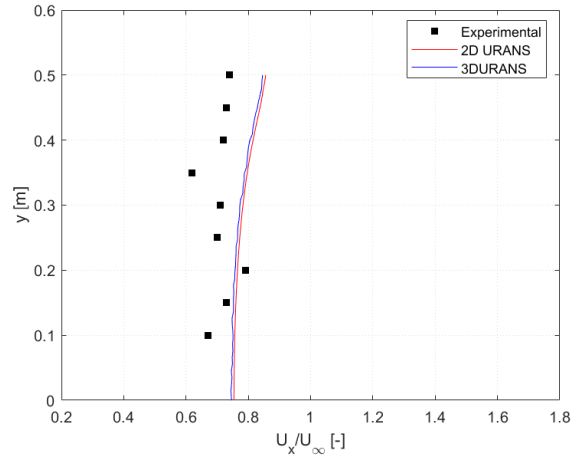
Figure 6. Comparison of dimensionless velocity profile vs radius from centerline between the experimental data and the CFD findings shown for DonQi®DWT model in non-yawed inflow condition.

Table 1. Grid statistics for grid independence study of the reference case.

Grid	Number of cells	C_{T_D}
Coarse	67640	0.3012
Medium	102008	0.3133
Fine	161028	0.3135

5 Results and Discussion

5.1 Duct geometries

Two duct geometries, shown in Figure 7, with different longitudinal cross section (named as DonQi® and DonQi D5) are chosen for the current investigation. The selection is based on the duct shape parametrization study conducted by the authors (Dighe et al., 2019b). The parametrization procedure for duct shapes preserved the following geometric features: leading edge position (which defines the inlet area ratio), trailing edge position (which defines the exit area ratio) and inner side thickness (which preserves AD radius and clearance). This makes it ideal to isolate the effects of the duct cross-section on the aerodynamic performance of the duct-AD model in yaw. In the study, an optimal $C_{T_{AD}} = 0.7$ was obtained for both the duct geometries. This value is employed for the rest of the discussion.

5.2 Duct force coefficient

Figure 8 illustrates the variation of duct force coefficient C_{T_D} as a function of yaw angle α obtained for the two duct geometries investigated in this study. Starting with the C_{T_D} trend-line for DonQi® duct, it can be observed that, C_{T_D} decreases with
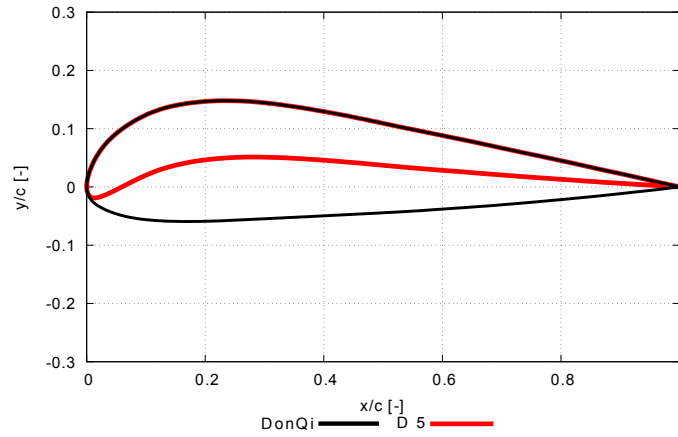
Figure 7. Cross-sectional geometry of the lower duct used for the numerical study.
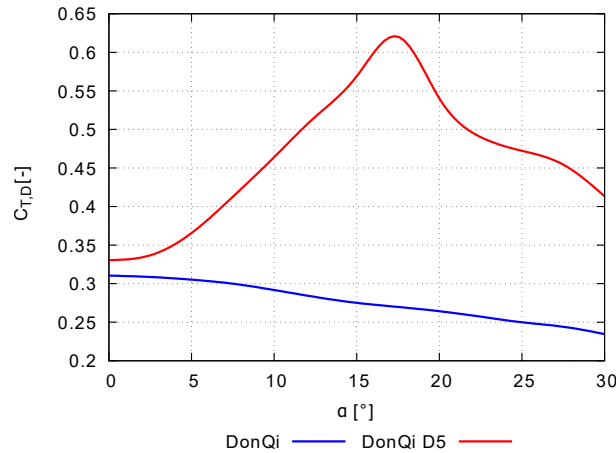
Figure 8. Effect of yawed inflow on the duct thrust force coefficient for the two duct geometries. $C_{T,AD} = 0.7$.

increasing values of α. Conversely, for DonQi D5 duct, C_{T_D} increases with increasing α. A local C_{T_D} maximum at $\alpha = 17.5°$ appears for the DonQi D5 duct. The value of C_{T_D} for DonQi D5 duct decreases for α beyond the local maximum.

The differences in the C_{T_D} trend-lines for the two duct geometries can be explained by looking at the flow field. Contours of non-dimensional free-stream velocity $\frac{U_x}{U_\infty}$ for both duct geometries are reported in Figures 9 (a) to (h). A range of yaw angles

5 have been tested, however, four yaw angles, i.e. $\alpha = 0°$, $10°$, $17.5°$ and $20°$, are presented here for the sake of conciseness. The velocity contours for DonQi® duct profile show that, with increasing values of α, the magnitude of velocity on the suction side of the duct decreases and the magnitude of velocity on the pressure side of the duct starts to increase significantly. Increasing the yaw angle causes flow separation on the suction side of the duct. At $\alpha = 20°$, the flow is completely separated, both on the suction and the pressure side, and the duct is fully stalled. The onset of inner duct wall flow separation is characterized by a

10 strong reduction of duct wall shear stress, which results in the reduction of C_{T_D} with increasing α as shown in Figure 8. For
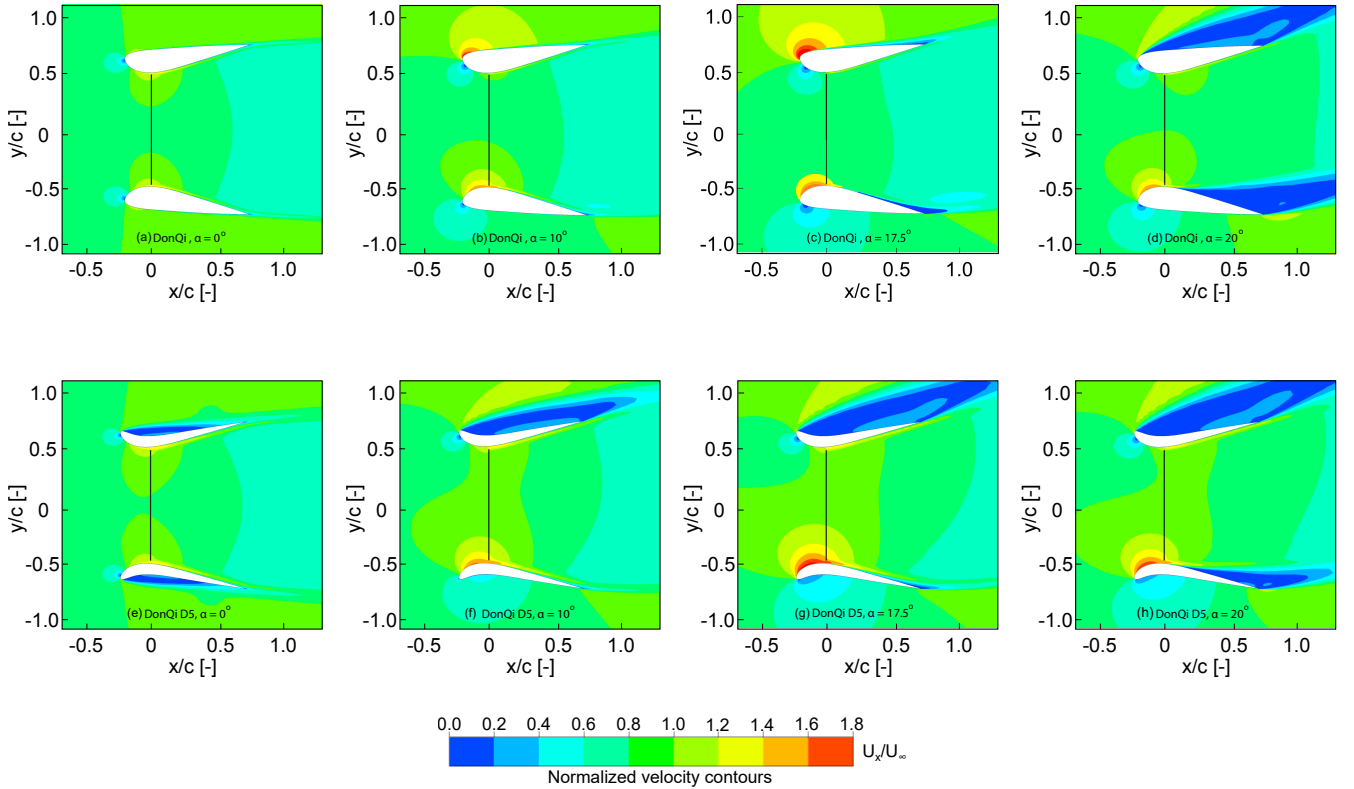
Figure 9. Velocity contours colored with streamwise normalized velocity. The results are depicted for DonQi duct-AD model (top) and DonQi D5 duct-AD model (bottom), both bearing a constant $C_{T,AD} = 0.7$.

the DonQi D5 duct, however, increased yaw returns higher velocity magnitude at the suction side of the duct up to $\alpha = 17.5°$. This is due to the duct profile camber, which promotes flow acceleration on the suction side of the duct. The increased velocity magnitude on the suction side of the duct in this range is always accompanied by flow separation on the pressure side of the duct. As long as the flow separation is limited to the pressure side, the integral of duct thrust force coefficient C_{T_D} in Figure 8 increases up to $\alpha = 17.5°$. At $\alpha = 20°$, the flow separation region traverses from the pressure side to the suction side of the duct indicating duct stalling characterized by the reduction of C_{T_D} in Figure 8.

5.3 Power Coefficient

Figure 10 represents the power coefficient C_P, for the two duct configurations, as a function of yaw angle α. For the sake of completeness, C_{P_o} for a bare AD is plotted alongside. The figure shows that, C_P is higher than C_{P_o} for all values of α. Comparing Figures 8 and 10, the C_P trends corresponds with the C_{T_D} trends. The larger the C_{T_D}, the higher the C_P reached, and vice-versa. Similar to the C_{T_D} trend for DonQi D5, maximum $C_P \approx 0.84$ is obtained for the DonQi D5 duct at $\alpha = 17.5°$; thereafter any further increase in α results in C_P drop. This also explains the experimental observations from Igra
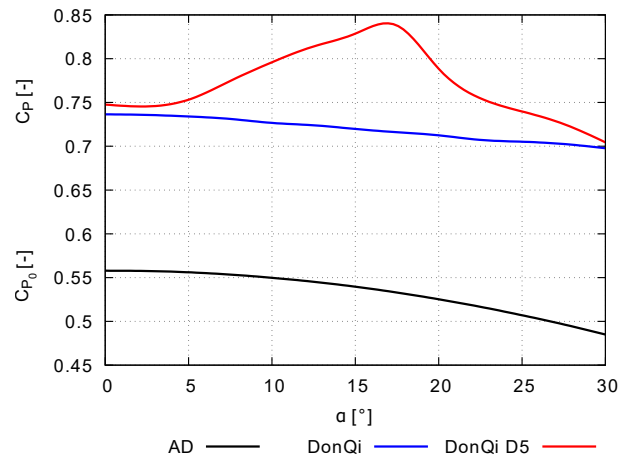
Figure 10. Effect of yawed inflow on the power coefficient.

(1981), where a drop in the power coefficient for the duct-AD models with large duct expansion ratio was observed. For high duct expansion ratio, the likelihood of flow to separate from the inner walls of the duct increases (Abe and Ohya, 2004), thus lowering the C_{T_D} and C_P values for a given duct-AD model.

6 Conclusions

5 The present article reignites the insights of Igra (1981) and Gilbert and Foreman (1983) to study the effects of yaw on the performance of DWTs. Based on the numerical predictions, the aerodynamic performance of DWTs in yawed flow:

- depend on the distinct shape of the duct under consideration.

- improves by increasing the duct profile camber. The duct camber acts as a flow conditioning device and delays duct wall flow separation on the suction side for a broad range of yaw angles.

Appendix A: Numerical verification of the duct-AD model.
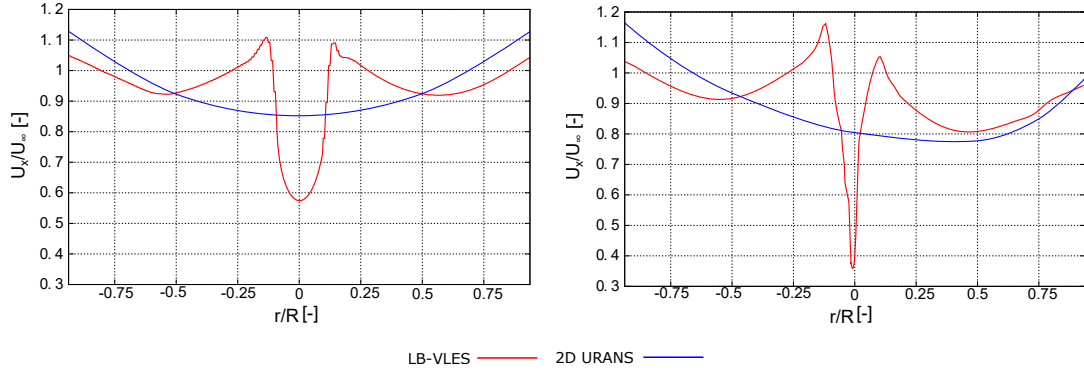
Figure 11. Radial distribution of streamwise velocity U_x/U_∞ located just aft of the turbine/AD plane.
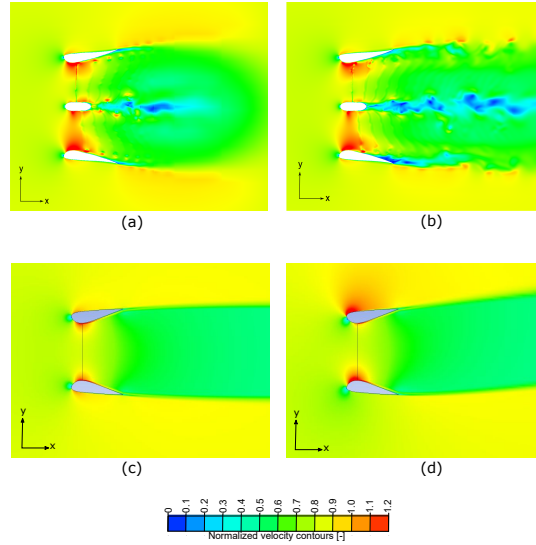
Figure 12. Contours of instantaneous streamwise velocity U_x/U_∞ in the $x - y$ plane for (a) DonQi® at $\alpha = 0$ degrees using LB-VLES approach, (b) DonQi® at $\alpha = 7.5$ degrees using LB-VLES approach, (c) DonQi® at $\alpha = 0$ degrees using 2D URANS approach and (d) DonQi® at $\alpha = 7.5$ degrees using 2D URANS approach.

Three-dimensional Lattice-Boltzmann Very Large Eddy Simulations (LB-VLES) of DWTs, where the rotor is simulated, in axial and yawed inflow conditions, forms the reference for the verification of the numerical approach presented in this article. For a detailed description of the LB-VLES approach, the reader can refer to Dighe et al. (2020). The baseline DonQi® DWT model is simulated for $\alpha = 0°$ and $7.5°$. The free-stream velocity is $U_\infty = 5$ m/s, which corresponds to Reynolds number $Re =$

3.31×10^5. Based on a previous study by Avallone et al. (2020), the resulting average rotor thrust coefficient equals 0.8; this value is adopted for specifying the input for the AD model.

Figure 11 examines the streamwise velocity component as a function of radial position using the two numerical approaches, both under non-yawed and yawed flow conditions. Before beginning this discussion, it must the stressed that the LB-VLES approach consists of turbine blades that are connected to a hub (upstream) and a nacelle (downstream). This geometric feature is not included in the duct-AD model; see Figure 12 (c) and (d). Despite this source of uncertainty, the overall computed $\frac{U_x}{U_\infty}$ trends show good agreement. As a testimony to model skewed wake, as seen in Figure 12 (d), the 2D URANS duct-AD approach exhibits a strong potential to implicitly model the flow around a DWT in yaw. The proposed simplified approach thus captures first order flow physics; for higher order effects, the blade shape resolving models will be well suited.

Author contributions. VVD compiled the literature review, setup the CFD simulations and wrote the bulk of the paper. DS performed the CFD simulations, post-processed the cases and contributed towards writing this paper. FA reviewed the paper and carried out modifications in different sections of this paper. GVB helped formulate the ideas in regular group discussions.

Competing interests. The authors declare that they have no conflict of interest.

5 *Acknowledgements.* Authors would like to acknowledge Prof. Ozer Igra for providing the experimental data that have contributed to the part of numerical validation reported in this paper. The research is supported by STW organization, grant number- 12728

References

Abe, K., Nishida, M., Sakurai, A., Ohya, Y., Kihara, H., Wada, E., and Sato, K.: Experimental and numerical investigations of flow fields behind a small wind turbine with a flanged diffuser, Journal of Wind Engineering and Industrial Aerodynamics, 93, 951–970, 2005.

Abe, K.-i. and Ohya, Y.: An investigation of flow fields around flanged diffusers using CFD, Journal of wind engineering and industrial aerodynamics, 92, 315–330, 2004.

ANSYS, I.: ANSYS ICEM CFD user's manual 18.0, ANSYS Inc., Canonsburg, Pennsylvania, USA, 2018.

Apsley, D. and Leschziner, M.: Advanced turbulence modelling of separated flow in a diffuser, Flow, Turbulence and Combustion, 63, 81, 2000.

Avallone, F., Ragni, D., and Casalino, D.: On the effect of the tip-clearance ratio on the aeroacoustics of a diffuser-augmented wind turbine, Renewable Energy, 152, 1317–1327, 2020.

Dighe, V. V., Avallone, F., Igra, O., and Bussel, G. v.: Multi-element ducts for ducted wind turbines: a numerical study, Wind Energy Science, 4, 439–449, 2019a.

Dighe, V. V., de Oliveira, G., Avallone, F., and van Bussel, G. J.: Characterization of aerodynamic performance of ducted wind turbines: A numerical study, Wind Energy, 2019b.

Dighe, V. V., Avallone, F., and van Bussel, G.: Effects of yawed inflow on the aerodynamic and aeroacoustic performance of ducted wind turbines, Journal of Wind Engineering and Industrial Aerodynamics, 201, 104 174, 2020.

Dupont, E., Koppelaar, R., and Jeanmart, H.: Global available wind energy with physical and energy return on investment constraints, Applied Energy, 209, 322–338, 2018.

Foreman, K. and Gilbert, B.: A Free Jet Wind Tunnel Investigation of DAWT Models, Grumman research and development Center Report to SERI, RE-668 (SERI/TR 01311-1), 1983.

Gielen, D., Boshell, F., Saygin, D., Bazilian, M. D., Wagner, N., and Gorini, R.: The role of renewable energy in the global energy transformation, Energy Strategy Reviews, 24, 38–50, 2019.

Gilbert, B. and Foreman, K.: Experiments with a diffuser-augmented model wind turbine, Journal of Energy Resources Technology, 105, 46–53, 1983.

Igra, O.: Research and development for shrouded wind turbines, Energy Conversion and Management, 21, 13–48, 1981.

Khamlaj, T. and Rumpfkeil, M.: Theoretical Analysis of Shrouded Horizontal Axis Wind Turbines, Energies, 10, 38, 2017.

de Vries, O.: Fluid dynamic aspects of wind energy conversion, Tech. rep., Advisory Group for Aerospace Research and Development NEUILLY-SUR-SEINE (France), 1979.

Mikkelsen, R. and Sørensen, J.: Yaw analysis using a numerical actuator disc model, in: Proceedings of 14th IEA Symposium on the Aerodynamics of Wind Turbines, FFA, 14th IEA Symposium on the Aerodynamics of Wind Turbines ; Conference date: 04-12-2000 Through 05-12-2000, 2001.

Phillips, D., Richards, P., and Flay, R.: CFD modelling and the development of the diffuser augmented wind turbine, Wind and Structures, 5, 267–276, 2002.

Shen, W. Z., Zhang, J. H., and Sørensen, J. N.: The actuator surface model: a new Navier–Stokes based model for rotor computations, Journal of solar energy engineering, 131, 2009.

Shives, M. and Crawford, C.: Developing an empirical model for ducted tidal turbine performance using numerical simulation results, Proceedings of the Institution of Mechanical Engineers, Part A: Journal of Power and Energy, 226, 112–125, 2012.

Tang, J., Avallone, F., and van Bussel, G.: Experimental study of flow field of an aerofoil shaped diffuser with a porous screen simulating the rotor, International Journal of Computational Methods and Experimental Measurements, 4, 502–512, 2016.

Ten Hoopen, P.: An Experimental and Computational Investigation of a Diffuser Augmented Wind Turbine: with an application of vortex generators on the diffuser trailing edge, 2009.

5 Tongchitpakdee, C., Benjanirat, S., and Sankar, L.: Numerical simulation of the aerodynamics of horizontal axis wind turbines under yawed flow conditions, Journal of Solar Energy Engineering-Transactions of The ASME, 127, 464–474, 2005.

Toshimitsu, K., Nishikawa, K., Haruki, W., Oono, S., Takao, M., and Ohya, Y.: PIV measurements of flows around the wind turbines with a flanged-diffuser shroud, Journal of Thermal Science, 17, 375–380, 2008.

Troldborg, N.: Actuator line modeling of wind turbine wakes, 2009.

10 van Bussel, G.: The science of making more torque from wind: Diffuser experiments and theory revisited, Journal of Physics: Conference Series, 75, 120–10, 2007.

Werle, M. and Presz, W.: Ducted wind/water turbines and propellers revisited, Journal of Propulsion and Power, 24, 1146–1150, 2008.